Zinc Stabilized Cation Ordered Chalcopyrite Thin Film for Enhanced Thermoelectric Power Generation Near Room Temperature

Hong Pang,[a] Cédric Bourgès,[b] Naohito Tsujii,[a] Rajveer Jha,[a] Naoyuki Kawamoto,[c] Fumihiko Ichihara,[d] Takahiro Baba,[a] Tetsuya Baba,[a] Naoki Sato,[a] Yuichi Yamasaki,[e] and Takao Mori*[af]

a. Research Center for Materials Nanoarchitectonics (MANA), National Institute for Materials Science (NIMS), Namiki 1-1, Tsukuba 305-0044, Japan

b. International Center for Young Scientists (ICYS), National Institute for Materials Science (NIMS), 1-1 Namiki, Tsukuba, 305-0044, Japan

c. Research Center for Advanced Measurement and Characterization, National Institute for Materials Science (NIMS), Namiki 1-1, Tsukuba 305-0044, Japan

d. Center for Green Research on Energy and Environmental Materials, National Institute for Materials Science (NIMS), Namiki 1-1, Tsukuba 305-0044, Japan

e. Research and Services Division of Materials Data and Integrated System (MaDIS), National Institute for Materials Science (NIMS), Sengen 1-2-1, Tsukuba 305-0047, Japan

f. Graduate School of Pure and Applied Sciences, University of Tsukuba, Tennoudai 1-1-1, Tsukuba 305-8671, Japan

Corresponding Author: MORI.Takao@nims.go.jp

Abstract

Multinary sulfides represent a significant family in semiconductors for their low cost and promising performance, yet controlling their composition is challenging. $CuFeS_2$ thin films are particularly attractive because of their great potential in thermoelectricity and photovoltaic. Herein we reveal the newest finding that Zn promotes the cation ordering and stabilizes the chalcopyrite $CuFeS_2$ film, preventing the reverse transformation to wurtzite with a random distribution of Cu-Fe at high temperature. The thermoelectric properties of chalcopyrite thin films are investigated as a function of Zn content, resulting in an optimized power factor of 0.168 $mW/m \cdot K^2$ at room temperature, outperforming any $CuFeS_2$ thin films ever reported. For the first time, synchrotron-based *in situ* X-ray diffraction and X-ray absorption fine structure confirm the phase transition, offering insights into the isomeric structure of $CuFeS_2$ and the role of Zn. The in-depth understanding of cation-ordering and phase transformation between $CuFeS_2$ polymorphs might impact the multinary sulfide film fabrication and efficiency improvement of renewable energy applications.

The ever-increasing consumption and demand for renewable energy have driven the research to explore the sustainable and environmentally friendly energy resources. For several decades work on the thermoelectric materials have rapidly grown to recover the waste heat and generate electricity.[1, 2] Defined by $ZT=\sigma S^2T/\kappa$, where σ is the electrical conductivity, S is the Seebeck coefficient, κ is the thermal conductivity, and T is the working temperature, the figure of merit of a thermoelectric material can be enhanced by different approaches[3, 4], namely, increasing S, σ or decreasing κ. Among various strategies, thin film has been recognized as a promising way to boost the ZT value by reducing κ due to geometrical confinement quantum effect and the increased interfacial/boundary phonon scattering[5-7]. As a case of high surface-to-volume structure, thin film may also possess different chemical and physical properties of the materials including electron transport, magnetism, phonon scattering, light absorption and so forth[8-11].

The family of I-III-S(Se/Te)$_2$ semiconductors, where group I attributed to coinage metal elements, have sparked interest in dual fields of thermoelectric and photovoltaic[12-14]. Cu–S systems represents a gallery of compositions and polymorphism, including $CuFeS_2$[15-23], $CuInS_2$[24, 25], $CuGaS_2$[12], etc., the majority of which have matchable bandgaps with solar spectrum and high absorption coefficients.[26] With the iron element, $CuFeS_2$ is a very special case due to the deep trap energy states by Fe 3d that create the nonradiative pathways of the photoexcited electrons relaxation and weak ferromagnetic property[26]. Compared with the conventional tellurides or antimonides, they do not depend on rare metals with limited reserve or toxicity. The large abundance of Cu, Fe and S in the earth's crust presents significant promise and advantage for scale-up. $CuFeS_2$ can be employed as an efficient photothermal and thermoelectric converters[26, 27].

The tetragonal chalcopyrite $CuFeS_2$ is a thermodynamically stable, *n*-type thermoelectric material with a suitable narrow bandgap. Due to its natural abundance and relatively high power factor, it is considered a promising candidate for thermoelectric applications. The strong coupling between electrons and magnetic moments in $CuFeS_2$ significantly enhances its effective mass, leading to remarkable thermoelectric power factor[28,29]. However, its intrinsic diamondoid lattice contributes to high κ, which limits further improvements in thermoelectric performance[30]. The lattice thermal conductivity (κ_l) is directly related to the phonon mean free path (l) through the equation $\kappa_l = 1/3Clv$, where C is the heat capacity and v the

phonon group velocity. Thus, shortening l can reduce κ_l. Besides methods such as introducing interstitial atoms, nano-precipitates and point defects to increase phonon scattering[21,22, 31], thin film fabrication is proposed as another viable approach to decrease κ[5]. Compared to bulk materials sintered at high temperatures and pressures, which generally feature grain sizes in the micrometer (μm) range, thin films with sub-micrometer thickness can significantly reduce the phonon l and, consequently, the κ. Additionally, recent advances in wearable electronics drive interest in thermoelectric films. Although $CuFeS_2$ thin films show great potential, research in this area remains limited.

Electrodeposition[32], flash evaporation[33], co-reduction[34], aerosol-assisted chemical vapor deposition (AACVD)[35], and sulfurization of CuFe alloys[36] have been utilized to prepare $CuFeS_2$ films. Compared with these conventional methods, magnetron sputtering was recognized unsuitable due to the harsh conditions and high particle energy[37]. However, the sputtering operated far from the equilibrium conditions, somehow favors the growth of the metastable phase[38], with a high formation enthalpy. The plasma-assisted magnetron sputtering deposition, in particular, offers several advantages: it produces continuous compact and dense films with uniform thickness, high crystallinity, with strong adhesion to the substrate, even at lower temperature, resulting in significantly higher electrical conductivity and improved thermoelectric properties. Moreover, the crystallite grains formed by magnetron sputtering are considerably smaller, typically in the nanometer range, in contrast to the micrometer scale produced by other techniques. This reduced grain size potentially introduces more grain boundaries, which contribute to phonon scattering, and lower thermal conductivity. Magnetron sputtering also avoids the need for a sulfur atmosphere chamber, sidestepping potential technical or regulatory barriers in many labs and reducing risks of pollution and safety hazards.

Our previous report shows the difficulty to obtain pure chalcopyrite $CuFeS_2$ phase during low-pressure magnetron sputtering by tuning the stage temperature as the elusive wurtzite phase appeared above 473 K[39]. Herein, it was found that incorporating Zn enables a complete phase transformation from cation disordered wurtzite to cation-ordered chalcopyrite, which obtained the highest thermoelectric performance among $CuFeS_2$-based thin films to the best of our knowledge. Insights in the conversion between the wurtzite and chalcopyrite phase and the Zn effect on the cation ordered $CuFeS_2$ structure are given, which is significant

for the growth of the multinary chalcogenide, especially I-III-S(Se/Te)$_2$ compound film application in energy conversion technologies.

$CuFeS_2$ thin films with different Zn contents were fabricated by the co-sputtering deposition using $Zn_{0.01}Cu_{0.99}FeS_2$, $Zn_{0.03}Cu_{0.97}FeS_2$ and $Zn_{0.05}Cu_{0.95}FeS_2$ chalcopyrite targets and a supplementary Cu target at varying substrate temperatures (373 K, 473 K, 573 K and 673 K). XRD patterns in **Figure 1a-c** show that the wurtzite (101) peak disappeared at 673 K for the films from the target $Cu_{0.99}Zn_{0.01}FeS_2$, $Cu_{0.97}Zn_{0.03}FeS_2$, while became indiscernible at 573 K for the film from $Zn_{0.05}Cu_{0.95}FeS_2$ target. XRD Rietveld refinement using the RIETAN-FP[40] reveals more information on the lattice parameters and the phase fraction (**Table S1-2**, **Figure S1**), confirming the higher substrate temperature increases the fraction of chalcopyrite. The refinement was carried out with the preferred orientation of (102) for wurtzite phase. At 673 K, films with different Zn levels are completely chalcopyrite. No significant differences in lattice parameters were observed due to the comparable atomic radius of Cu and Zn cations.

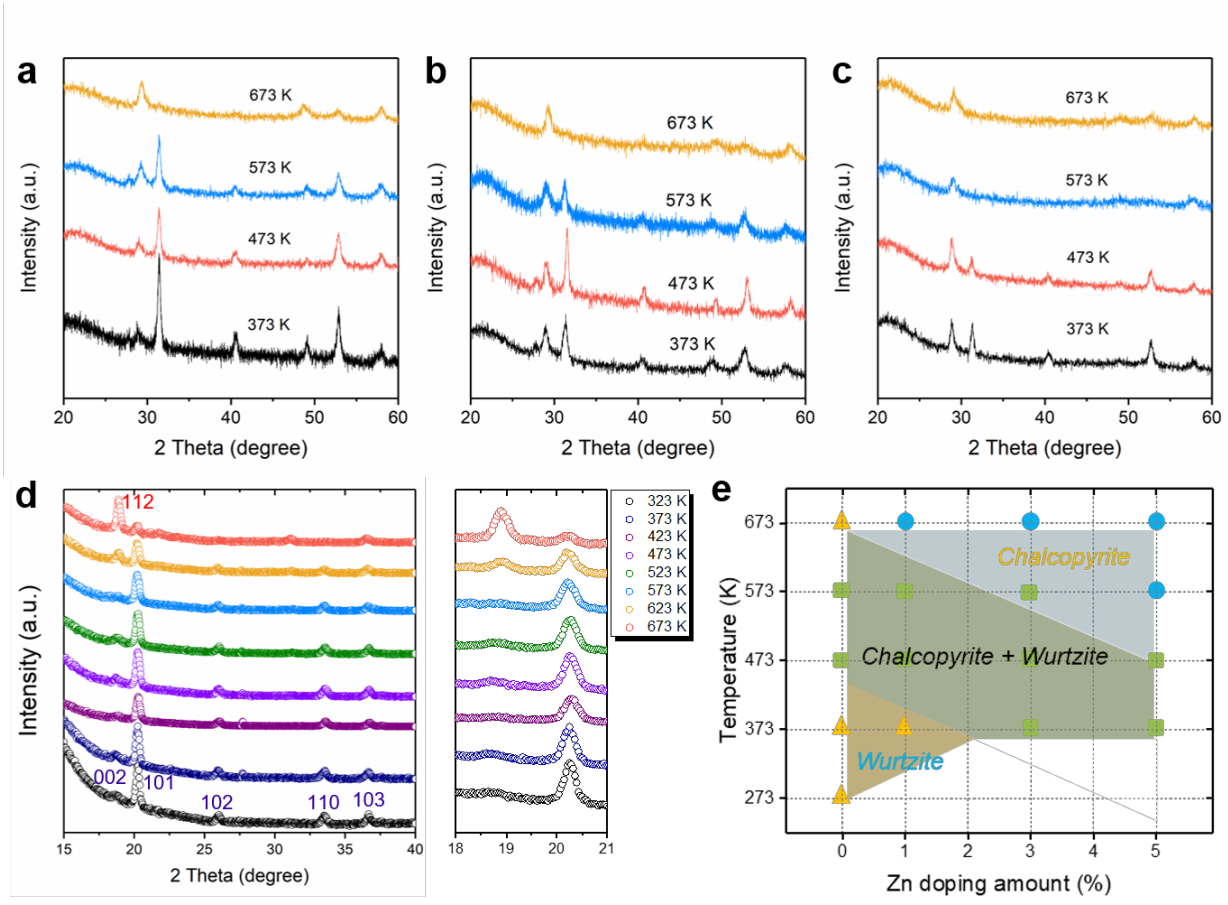

Figure 1. The laboratory-based XRD patterns of the co-sputtered thin films derived from (a) $Zn_{0.01}Cu_{0.99}FeS_2$, (b) $Zn_{0.03}Cu_{0.97}FeS_2$ and (c) $Zn_{0.05}Cu_{0.95}FeS_2$ chalcopyrite targets on quartz substrates at different temperature (373 K, 473 K, 573 K and 673 K) using λ_{Cu}= 1.5406 Å. (d) Synchrotron-based *in situ* XRD measurements data collected from 323 K to 673 K with an interval of 50 K on the film deposited from $Zn_{0.01}Cu_{0.99}FeS_2$ target (Right panel: the enlarged range of 18°-21°) using λ= 1 Å. (e) Growth parameter-based phase diagram of $Zn_xCu_{1-x}FeS_2$ films (triangle: wurtzite; circle: chalcopyrite; square: mixture of wurtzite and chalcopyrite).

The phase transformation was further investigated using synchrotron-based *in situ* grazing-incidence X-ray diffraction (GIXRD) measurement. The film deposited at room temperature using the $Zn_{0.01}Cu_{0.99}FeS_2$ target was examined. The XRD peaks at 18.6° and 20.2° (**Figure 1d)** in the range of low temperatures can be indexed to the (002) and (101) of the wurtzite structure with a space group of $P6_3mc$ (no.186). When temperature elevated, the intensity of the predominant peak (101) in wurtzite decreased while the intensity at 18.9°, aligning with (112) in chalcopyrite, increased, signifying the gradual disappearance of hexagonal wurtzite structure and the formation of chalcopyrite. This phenomenon serves as the direct evidence of the transformation from wurtzite into chalcopyrite. Upon heating to 673 K and maintaining for several minutes, the wurtzite structure fully converted into chalcopyrite, implying that the phase transformation is thermally activated and requires a substantial activation energy that can be reduced by Zn. Based on the phase variation with Zn dopant content and temperature, a simplified phase diagram was figured out in **Figure 1e**.

SEM analysis (**Figure S2**) of the films deposited at various temperature are presented, with the representative chalcopyrite film using $Zn_{0.01}Cu_{0.99}FeS_2$ at 673K shown in **Figure 2a**. The average crystallite sizes after calibrating the FWHM curve using MDI Jade were listed in Table S3, which suggests the wurtzite has larger crystallite size than the chalcopyrite formed at higher temperature. The sizes are comparable to the particles observed by SEM. However, in SEM, as Zn increases, the morphology at 673 K shifts from the angular nanoplates to the nanospheres without apparent arris. As temperature increases, crystals form a

corner perpendicular to the plates, evolving into larger particles. This is rationalized by the faster growth rate of wurtzite crystal in the *c*-axis, driven by a closely packed stacking mode. Higher temperature facilitated the transformation from wurtzite to chalcopyrite, reducing the anisotropic characteristic of wurtzite and promoting a balance between *a*-axis and *b*-axis orientation.

The role of Zn in chalcopyrite was unravelled to create ZnS island to decrease κ[21]. But our elemental mapping in **Figure S3** failed to distinguish the existence of ZnS, contrary to the previous report. Energy dispersive X-ray (EDX) mapping in **Table S4** corresponding to the films deposited at 673 K with varying Zn amount, shows Cu:Fe:S ratios close to the stoichiometric 1:1:2 of chalcopyrite, with deviation notably observed at higher Zn amount. We calculated the micro-strain, dislocation density and the stress as shown in **Table S5**[41-47]. From **Table S5**, it can be observed the generated film from $Zn_{0.05}Cu_{0.95}FeS_2$ has obviously larger dislocation density, micro-strain compared with the films from $Zn_{0.01}Cu_{0.99}FeS_2$ and $Zn_{0.03}Cu_{0.97}FeS_2$, which may relate to the higher off stoichiometry with more Zn involved and also the stress from the mismatch of thermal-expansion coefficient between the chalcopyrite ($7.2\sim9.0 \times10^{-6}$ K^{-1})[46] and quartz ($0.5\sim1.0\times10^{-6}$ K^{-1}).

To further analyze the microstructure, a portion of the film deposited with $Zn_{0.01}Cu_{0.99}FeS_2$ target at 673 K was tailored by focused ion beam (FIB) and thinned into 100 nm thickness for transmission electron microscopy (TEM) observation. The TEM image shows a compact, homogeneous morphology with lateral size ranging from 70 -100 nm (**Figure 2a**) and a thickness of 210 - 270 nm (**Figure 2b**). A pronounced textured orientation is evident at the cross-section (**Figure 2c**), due to the so-called "turbostratic" growth[48], consistent with 101 in wurtzite thin film[39]. The self-organized stacking behaviour spontaneously formed a columnar structure, especially when comparing the red marked convex area A and the yellow marked concave area B between two adjacent convexes in **Figure 2c**. The predominant crystal planes in the high-resolution TEM (HRTEM) of area A in **Figure 2d** indicates a 0.298 nm lattice distance, corresponding to the (112) crystal planes in chalcopyrite. The fast Fourier transformation (FFT) in **Figure 2e** confirms single-crystal grains with diffraction spots indexed to 112, 220 and 00$\bar{4}$, indicating the <112> orientation parallel to the columnar morphology. In area B (**Figure 2f**), strong stacking disorder and random orientation of the small grains was observed, which may enhance phonon scattering due to defects and lattice distortion.

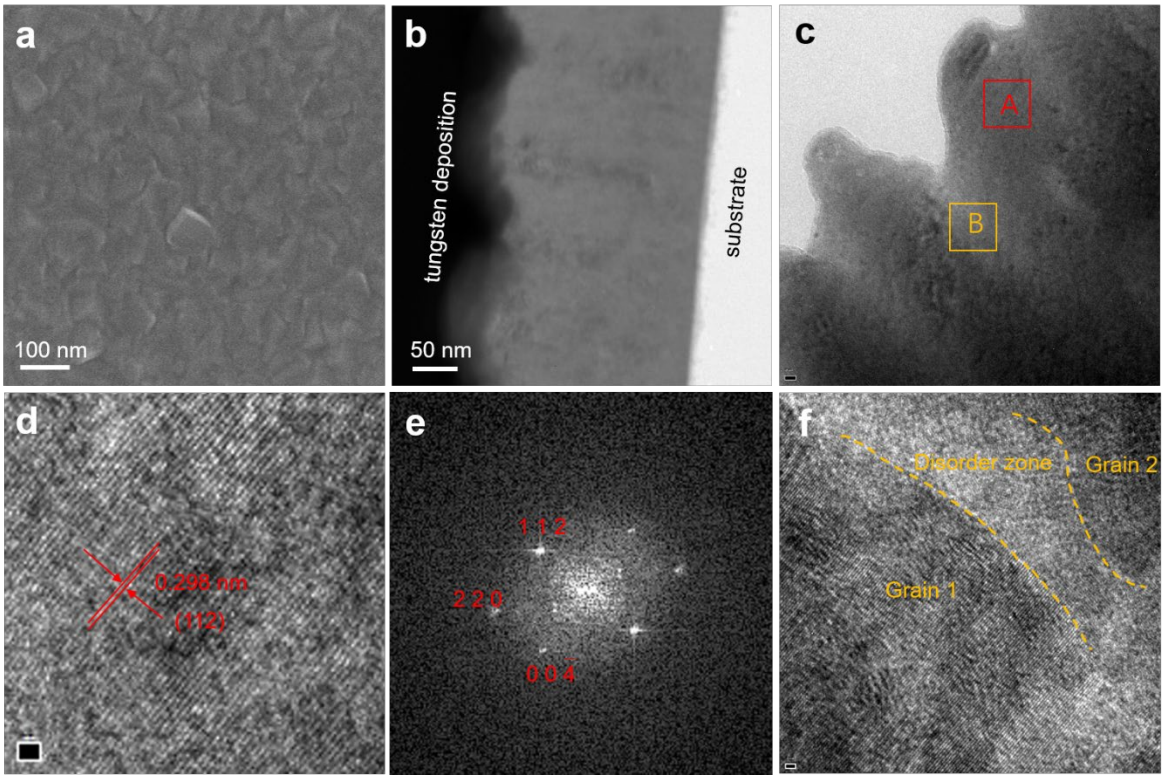

Figure 2. (a) Top view of the bright-field SEM image, (b) dark-field cross-section image, (c) bright-field cross section image, (d) high-resolution TEM image, (e) electron diffraction pattern corresponding to (d), and the image of the grain boundary from the TEM observations of the film deposited from $Zn_{0.01}Cu_{0.99}FeS_2$ target.

Chalcopyrite $CuFeS_2$, with the space group of *I*-42d (no.122), features with each S anion tetrahedrally coordinated to two Cu cations and two Fe cations. The Raman spectroscopy of the films in **Figure 3a** compares the wurtzite films deposited at 373 K and chalcopyrite film at 673 K utilizing $Zn_{0.03}Cu_{0.97}FeS_2$ target. Due to the symmetry of chalcopyrite containing two formulas per primitive unit cell, the optical vibrational modes can be decomposed into 15 modes: Γ1=A1(R) + 2A2 + 3B1(R) + 3B2 (R, IR) + 6E (R, IR), where A1 and B1 represents the nonpolar Raman active modes; A2 is an optical silent mode; B2 and E are polar Raman active modes, encompassing transverse optical, longitudinal optical mode, as well as the IR active modes[49].Associated with the motion of anions, A1 manifests the strongest peak among all the

modes. The chalcopyrite thin films show four typical Raman peak regions at 211.7–213.7 cm^{-1}, 274.0–276.6 cm^{-1}, 381.6–387.5 cm^{-1} and 471.3–483.8 cm^{-1}, the latter three of which can be assigned to the A1, B2 or E modes[50,51]. The peak observed at 214.7–217.9 cm^{-1} is linked to nanorod-textured $CuFeS_2$ with small diameters. Wurtzite ($P6_3mc$, no. 186) has vibrational modes Γ2=A1(R, IR) + E1(R, IR) + 2E2 (R) + 2B1, where B1 is silent mode; A1 and E1 mode are polar modes active for both Raman and IR. A1 and E1 are parallel and perpendicular to the *c*-axis, and both exhibits TO and LO modes due to the long-range electrostatic forces[52]. A meticulous analysis found that the LA peak at 213.7 cm^{-1} can be divided into 210.4 cm^{-1} and 219.4 cm^{-1}. The peak located at 276.6 cm^{-1} in chalcopyrite, where A1 and E1 are too close to be distinguished, can be deconvoluted into 266.3 cm^{-1} and 283.7 cm^{-1} in wurtzite structure. The decrease in the peak near 450 cm^{-1} is indicative of the less disorder in chalcopyrite at higher temperature than the wurtzite-type at lower temperature. The stoichiometric variation also affects the site occupancy and chemical environment in different crystal structures and the Raman modes. **Figure 3b** exhibited the chalcopyrite thin films deposited at 673 K with increasing Zn amount. The slight blue shifting of B2 peak, which is associated with the motion of cations, along with the new mode near 590 cm^{-1}, indicates the increasing amount of Zn.

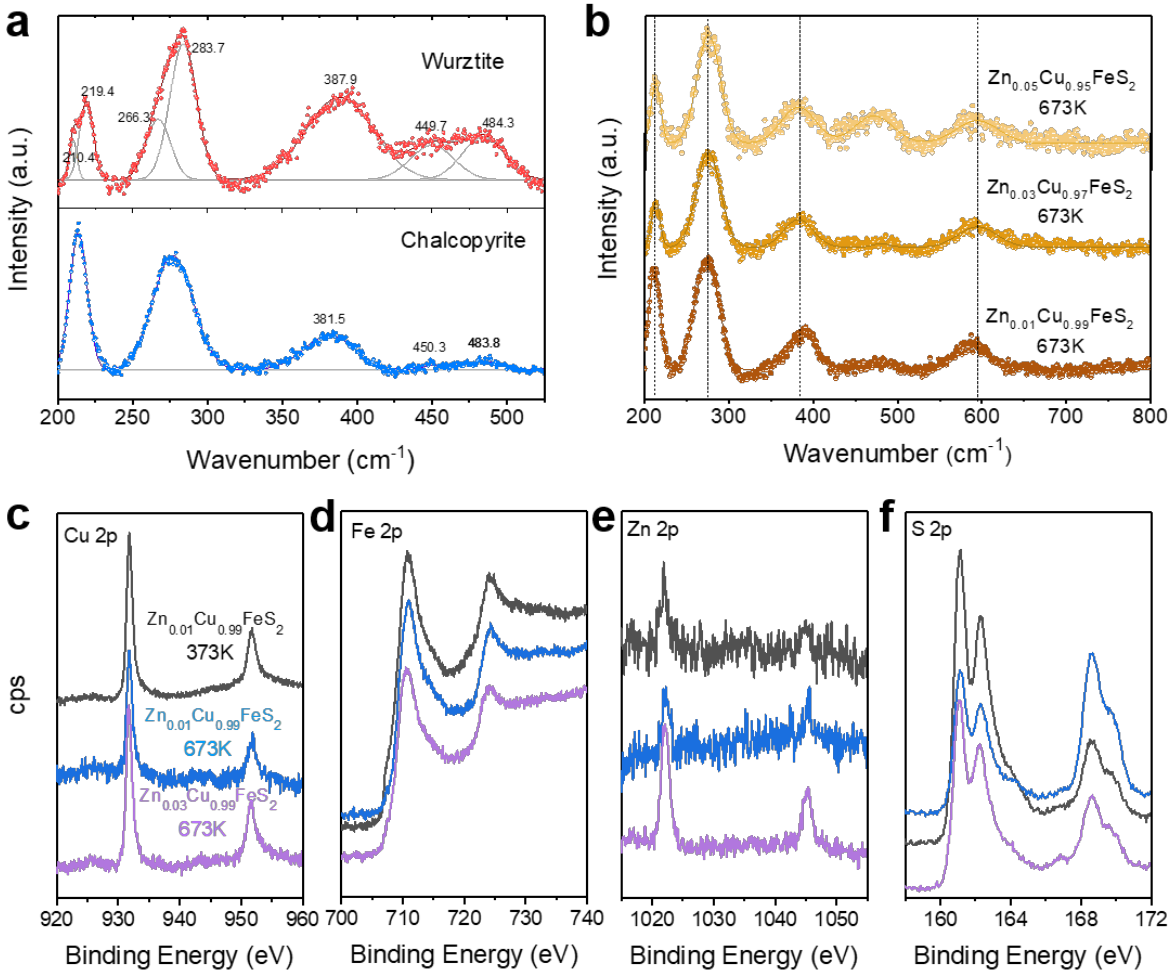

Figure 3. Raman spectra of (a) Wurtzite Zn-$CuFeS_2$ thin film deposited at 373 K and chalcopyrite Zn-$CuFeS_2$ thin film at 673 K using the target $Zn_{0.03}Cu_{0.97}FeS_2$ (b) Chalcopyrite Zn-$CuFeS_2$ thin films deposited at 673 K using the target $Zn_{0.01}Cu_{0.99}FeS_2$, $Zn_{0.03}Cu_{0.97}FeS_2$ and $Zn_{0.05}Cu_{0.95}FeS_2$. High-resolution XPS spectra of (c) Cu, (d) Fe, (e) Zn, (f) S of the low-temperature (373 K) deposited wurtzite film and high-temperature (673 K) deposited chalcopyrite film from $Zn_{0.01}Cu_{0.99}FeS_2$ and $Zn_{0.03}Cu_{0.97}FeS_2$.

The valence state of Cu, Fe, Zn and S were assessed by X-ray photoelectron spectroscopy (XPS) by comparing the wurtzite film (373 K) and chalcopyrite film (673 K) from $Zn_{0.01}Cu_{0.99}FeS_2$ as well as the chalcopyrite film (673 K) from $Zn_{0.03}Cu_{0.97}FeS_2$ in **Figure 3c-f** with the peaks listed in **Table S6**. All films exhibit nearly identical positions for Cu 2*p* and Fe 2*p* peaks, indicating the predominant valence states of

Cu and Fe inherited from the chalcopyrite targets. In the high-resolution XPS spectra of Cu from wurtzite film (373 K) and chalcopyrite film (673 K) from $Zn_{0.01}Cu_{0.99}FeS_2$ in **Figure 3c**, there is no obvious shift of the peaks located at 931.8 eV and 951.7 eV, which belong to Cu $2p_{3/2}$ and Cu $2p_{1/2}$ of the monovalent Cu (Cu^+), respectively, indicating the identical local environment of Cu in wurtzite and chalcopyrite. However, Zn dopant shifts the binding energy of Cu to a higher direction. The Fe $2p_{3/2}$ and Fe $2p_{1/2}$ peaks situated at 710.7 eV and 724.0 eV of wurtzite film in **Figure 3d**, indicating a fully coordinated Fe ion (Fe^{3+}), shift to higher binding energy when the wurtzite type transformed into chalcopyrite but shifted to lower energy when increasing Zn dopant. Zn peak positions at 1021.8 eV and 1044.9 eV indicate the stable +2 oxidation status, suggesting increased electron carrier concentration after substituting the monovalent Cu. A dramatic increase from 1021.8 eV to 1022.1 eV from wurtzite to chalcopyrite indicates stronger Zn-S bonding. A further slight increase in Zn binding energy is observed from 1 % to 3 % substitution in **Figure 3e**. At the same time, the S 2*p* spectra (**Figure 3f**), demonstrate a blue shift of S $2p_{1/2}$ and S $2p_{3/2}$ peaks during the wurtzite-to-chalcopyrite transformation, but maintaining same valence state with Zn amount increasing.

The observations correlate well with the structure characteristic of wurtzite and chalcopyrite. In the case of wurtzite, Cu and Fe occupies the same position with 0.5 occupancy in a random distribution of cations. The bond length of three Cu (Fe)-S is 2.27 Å and another Cu (Fe)-S is 2.35 Å with the cell parameter a = 3.73 Å and c = 6.13 Å. In chalcopyrite with cell parameters a = 5.29 Å and c = 10.42 Å, the bond lengths of Cu-S and Fe-S are 2.30 Å and 2.26 Å, respectively. When the structure transforms from wurtzite to chalcopyrite, the fraction of shortened and elongated Cu-S bond might be equal, explaining the absence of a significant shift in Cu binding energy. However, the Fe-S was 100% shortened, justifying the increase of the Fe binding energy. With Zn increased, the Zn-S bonding becomes strengthened and Fe-S weakened, consistent with the shifts in Fe 2*p* and Zn 2*p* peaks.

Synchrotron-based X-ray absorption fine structure measurements were conducted to probe the local environment of the Cu, Fe and Zn atoms of the chalcopyrite $CuFeS_2$ films from the targets with different Zn at 673 K. X-ray absorption near-edge structure (XANES) in **Figure 4a-c**, shows no evident shift of the K-edge of the Cu, Fe and Zn. The white line peaks, reflecting the electronic structure and oxidation state,

show identical feature in Cu K-edge, Fe K-edge and Zn-edge spectra across all doping levels, confirming the valence state of Cu, Fe and Zn as +1, +3 and +2, respectively, in agreement with XPS results.

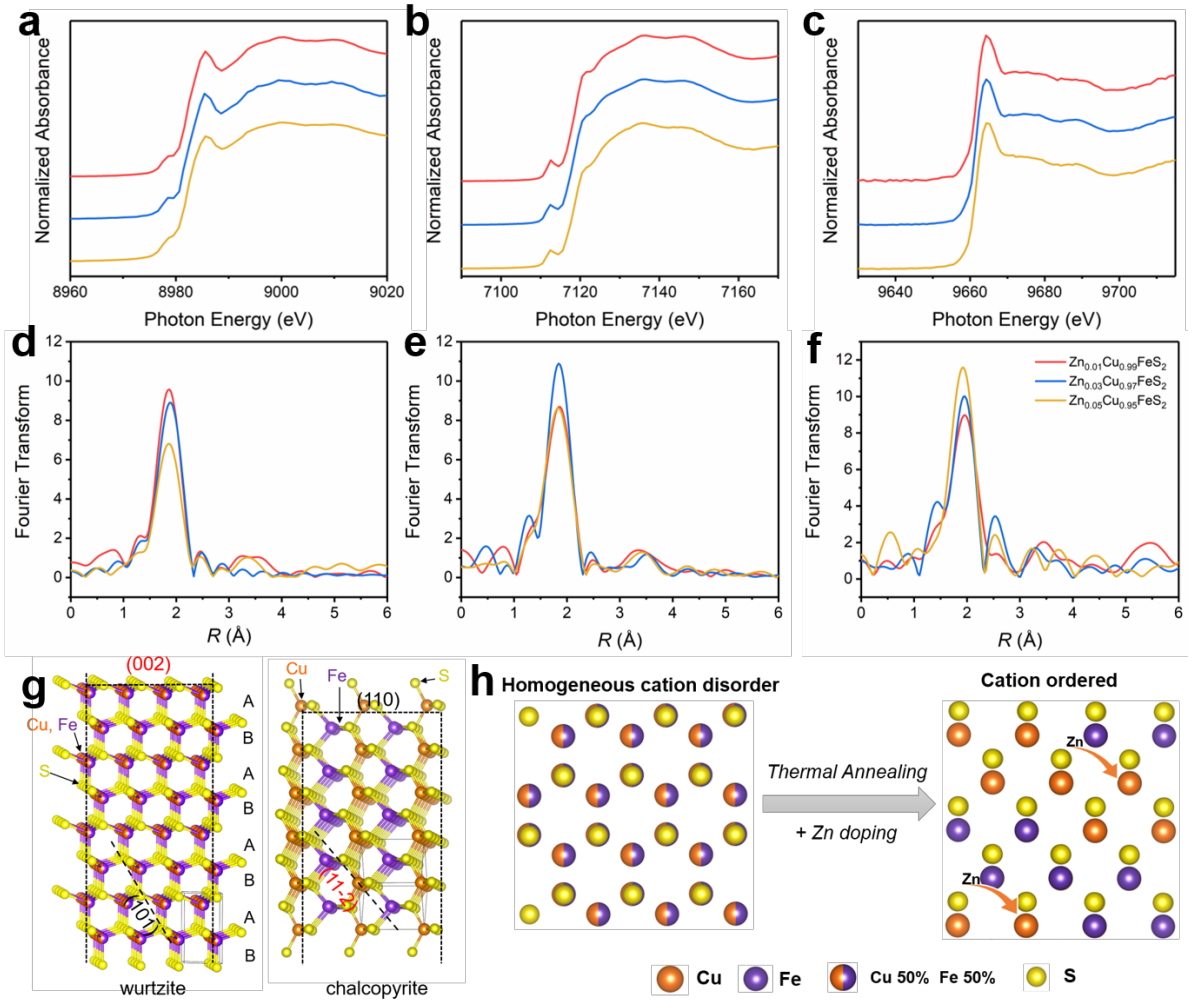

Figure 4. K-edge XANES spectra of (a) Cu (b) Fe (c) Zn and the associated Fourier transform of k^2-weighted EXAFS oscillations of (d) Cu (e) Fe (f) Zn of the chalcopyrite Zn-$CuFeS_2$ thin films deposited at 673 K using targets with different Zn amount. (g) Perspective view of crystal structure difference of $CuFeS_2$ for the transition from wurtzite to chalcopyrite (h) Projected view of wurtzite from zone-aixs [001] and chalcopyrite structure from zone-axis [110].

The Fourier transformation of the extended X-ray absorption fine structure (EXAFS) of Cu, Fe and

Zn in **Figure 4d-f**, represents the coordination environment. Fitting with the chalcopyrite structure (detailed in **Table S7)** reveals the S^{2-} anions are tetrahedrally coordinated to cations, forming metal-S bonds. Zn and Fe atoms have a relatively high coordination with $N > 3$; Cu atoms has the least coordination number, suggesting the S atoms are prone to bond with Zn/Fe to from the tetragonal ZnS_4/FeS_4 rather than CuS_4. The low coordination number of Cu implies a partial filling in the nearest-neighbor occupancies, suggesting the existence of sulfur vacancy. As Zn increase, the intensity of the first oscillation Cu-S shell decreases (**Figure 4d)** while Zn-S increases (**Figure 4f)**, strongly evidencing the substitution of Cu host occupancy by Zn.

It can be understood from the diatomic bond dissociation energy. Zn-S bonds (205 kJ/mol) are weaker and longer (by 0.04-0.08 Å) than Cu-S bond (285 kJ/mol)[53], creating local disorder and weakening the overall metal-S bond strength. The weaker bond promotes sulfur vacancy near Cu with increasing Zn level. The reduced coordination of Cu may facilitate the formation of Cu_xS, which act as the catalyst for the transformation from hexagonal closed packed (hcp) to face-centered cubic (fcc) structure[54]. This may explain the origin of the transformation of ternary wurtzite to chalcopyrite at high temperature. The phase transition can be seen as an atomic shift with the introduction of Zn atoms (**Figure 4g**). The growth along wurtzite <002> direction was converted to energetically preferred (112) planes, forming chalcopyrite. The Cu and Fe cations become ordered rather than randomly occupied (**Figure 4h**).

To elucidate the impact of Zn on the thermoelectric properties of the chalcopyrite $CuFeS_2$ thin film, the temperature-dependent electrical conductivity (σ) and Seebeck (S) coefficient of the films deposited at 673 K derived from $Zn_{0.01}Cu_{0.99}FeS_2$, $Zn_{0.03}Cu_{0.97}FeS_2$ and $Zn_{0.05}Cu_{0.95}FeS_2$ target have been investigated. **Figure 5a** shows σ of Zn-$CuFeS_2$ thin films increase with temperature ranging from room temperature to 523 K, indicating a semiconducting feature throughout the entire temperature regime, in accordance with the previous report on the electronic structure of the chalcopyrite $CuFeS_2$[18, 19]. Films with lower Zn amount exhibited relatively high σ (~10^3 S/m) while higher Zn amount led to one order of magnitude lower σ (2.9×10^2 S/m) at room temperature. The σ values of the previous two films are comparable with previously reported bulk counterpart[15], indicating the high quality of our co-sputtered sulfide films.

The charge carriers on the three films were investigated via Hall measurements at ambient conditions. Electrical conductivity depends on mobility and carrier concentration. As listed in **Table S4 and Figure 5d-e**, the electrons carrier concentration rises with higher Zn amount while the carrier mobility shows an opposite tendency. The incorporation of Zn into the $CuFeS_2$ host lattice results in Zn atom ionizing into Zn^{2+}, replacing one Cu atom and contributing one free electron to the carrier concentration. Simultaneously, it induces sulfur deficiency as identified by EXAFS. Consequently, the high carrier concentrations are associated with the intrinsic carriers (eg. sulfur defects) and extrinsic carriers (Zn). Chalcopyrite films from $Zn_{0.01}Cu_{0.99}FeS_2$ and $Zn_{0.03}Cu_{0.97}FeS_2$ exhibit enhanced carrier mobility compared to the undoped film, leading to improved electrical conductivity. In contrast, the mobility of film from $Zn_{0.05}Cu_{0.95}FeS_2$ dramatically decreased to 10^{-2} /$cm^2 \cdot V \cdot s$, likely due to the smaller grain size and increased boundaries where a large number of defects probably exist.

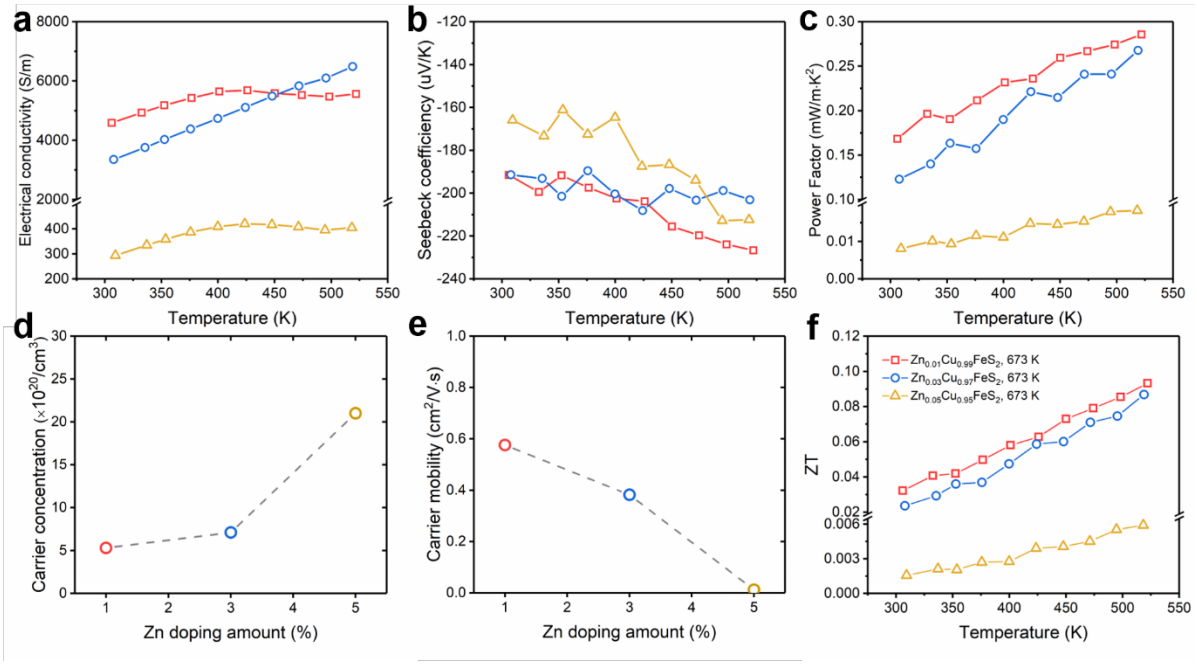

Figure 5. Thermoelectric properties: (a) Electrical conductivity (σ) (b) Seebeck coefficient (*S*) (c) Power factor (*PF*) of the chalcopyrite Zn-$CuFeS_2$ thin films deposited from the target $Zn_{0.01}Cu_{0.99}FeS_2$, $Zn_{0.03}Cu_{0.97}FeS_2$ and $Zn_{0.05}Cu_{0.95}FeS_2$ at 673 K. (d) Carrier concentration and (e) Carrier mobility measured

at room temperature of the chalcopyrite films deposited from different targets. (f) The estimated ZT assuming a constant value of thermal conductivity.

The Seebeck coefficient (*S*) was investigated as another indicator of thermoelectric property with regards to temperature. As shown in **Figure 5b**, the negative sign of the *S* suggests electrons as the predominant charge carriers in chalcopyrite films with its absolute value slightly increase with the temperature. Films from $Zn_{0.01}Cu_{0.99}FeS_2$ and $Zn_{0.03}Cu_{0.97}FeS_2$ exhibit similar values in all temperature range while *S* for the film from $Zn_{0.05}Cu_{0.95}FeS_2$ is much lower. Considering the actual substitution content of the two films from $Zn_{0.01}Cu_{0.99}FeS_2$ and $Zn_{0.03}Cu_{0.97}FeS_2$ are 2.92% and 3.20% by EDX, it is reasonable to observe similar *S* of -180 ~190 μV/K. The S_{max} at room temperature is -191 μV/K for the film from $Zn_{0.01}Cu_{0.99}FeS_2$, lower than the undoped $CuFeS_2$ thin film of -266 μV/K [34] and the previously reported bulk $Cu_{0.97}Zn_{0.03}FeS_2$ value [15-17]. Theoretical calculations implied a lower *S* for the doped film (~70 μV/K) due to its metallic nature.[19] However, our film exhibits a higher *S*, likely owing to the nanostructured grains.

As a result, **Figure 5c** shows the temperature-dependence of the power factor *PF* (σS^2). All films have a growing *PF* with temperature. The *PF* at room temperature is 0.168 mW/m·K^2, over 5-fold higher than that of the pristine $CuFeS_2$ (0.032 mW/m·K^2), and 7-fold than the previous reported flexible $Zn_{0.02}Cu_{0.098}FeS_2$/PEDOT:PSS/graphene film (0.023 mW/m·K^2)[55] (Comparison with the other $CuFeS_2$-based films in Table S8); the PF_{max}, 0.285 mW/m·K^2 is obtained at 523 K. The fabrication method was also extended to Kapton polyimide tape, a flexible substrate, resulting in a *PF* of 0.100 mW/m·K^2 at room temperature and 0.195 mW/m·K^2 at 523 K (**Figure S4**), indicating its potential in flexible low-temperature energy harvesters despite slightly lower performance.

Thermal conductivity (κ) was measured by picosecond time-domain thermoreflectance (TD-TR) method. The theoretical regression curve could be found in **Figure S5**, which gives a value of 1.6 W/m·K at room temperature, lower than the undoped $CuFeS_2$ film[39]. The total thermal conductivity (κ_t) includes the electronic (κ_e) and lattice (κ_l) contributions. According to the Wiedemann-Franz law, $\kappa_e = LT\sigma$, where *L* represents the Lorentz number that can be estimated from the equation L=1.5+exp[-|S|/116][56], the electronic

part is negligible compared with the total. The reduced κ is primarily attributed to the enhanced phonon scattering from massive grain boundaries and point defects in nanostructured films. The calculated ZT at near room temperature for the best chalcopyrite thin film is 0.032 (305K) and 0.040 (329 K), comparable to the bulk value (0.040 at 325 K)[21], which is the best value for ever reported $CuFeS_2$ thin films. Even though we have no data of the thermal conductivities at higher temperature, the temperature-dependent ZT is estimated by assuming a constant κ, in **Figure 5f**. The high-temperature and high-pressure preparation method for thermoelectric bulk materials results in significantly higher electrical conductivity, which also leads to higher thermal conductivity. In contrast, films with lower densification exhibit reduced electrical conductivity. However, their substantially lower thermal conductivity enables to achieve a comparable ZT value to that of bulk materials. The work indicates the chalcopyrite Zn-$CuFeS_2$ thin films serve as promising alternative to the thermoelectric applications with low thermal conductivity.

In summary, we fabricated chalcopyrite Zn-$CuFeS_2$ thin films via magnetron sputtering, finding that introduction of Zn stabilizes the chalcopyrite phase and prevents its reverse transformation to wurtzite at high temperature. By varying the Zn amounts and deposition temperature, the cation ordered chalcopyrite thin film was achieved with an enhanced power factor of 0.168 $mW/m \cdot K^2$ at room temperature and 0.285 $m \cdot K^2$ at 523 K. ZT of the optimized chalcopyrite thin film is comparable to the bulk $CuFeS_2$. This study showcased the first *in situ* synchrotron-based XRD demonstration of phase transformation from wurtzite to chalcopyrite in $CuFeS_2$. The work not only paves the way for the ternary I-III-S $(Se/Te)_2$ films but also advances understanding into cation modulation and ordering engineering in the multinary sulfide thin film fabrication.

Declaration of Competing Interest

The authors declare no conflict of interest.

Acknowledgment

This work was supported by JST Mirai Program Grant Number JPMJMI19A1. This research was undertaken with the approval of the Photon Factory Advisory Committee (Proposal number 2018S2-006,

2021G133).

Supporting Information

The Supporting Information is available free of charge at:

Experiments; scheme of co-sputtering; Rietveld refined profile, parameters and results; calculations from XRD; EDX; SEM; XPS; time-resolved thermoreflectance; EXAFS fitting results; properties comparison (PDF)

References

(1) Hendricks, T.; Caillat, T.; Mori. T. Keynote Review of Latest Advances in Thermoelectric Generation Materials, Devices, and Technologies. *Energies*, **2022**, *15*(19): 7307.

(2) Freer, R.; Powell, A.V. Realising the Potential of Thermoelectric Technology: a Roadmap. *J. Mater. Chem. C*, **2020**, *8*, 441-463.

(3) Mori, T. Novel Principles and Nanostructuring Methods for Enhanced Thermoelectrics. *Small*, **2017**, *13*(45): 1702013.

(4) Mao, J.; Liu, Z.; Zhou, J.; Zhu, H.; Zhang, Q.; Chen, G.; Ren, Z. Advances in Thermoelectrics. **2018**, *67*, 69-147.

(5) Venkatasubramanian, R.; Siivola, E.; Colpitts, T. O'Quinn, B. Thin-film Thermoelectric Devices with High Room-temperature Figures of Merit. *Nature*, **2001**, *413*(6856): 597-602.

(6) Baba, T.; Baba, T.; Ishikawa, K.; Mori, T. Determination of Thermal Diffusivity of Thin Films by Applying Fourier Expansion Analysis to Thermo-reflectance Signal after Periodic Pulse Heating. *J. Appl. Phys*., **2021**, *130*, 225107.

(7) Baba, T.; Baba, T.; Mori, T. Development of Fourier Transform Ultrafast Laser Flash Method for Simultaneous Measurement of Thermal Diffusivity and Interfacial Thermal Resistance. *Int. J. Thermophys.* **2024**, *45*, 27.

(8) Gao, W.; Liu, Z.; Baba, T.; Guo, Q.; Tang, D.; Kawamoto, N.; Bauer, E.; Tsujii, N.; Mori T. Significant Off-stoichiometry Effect Leading to the N-type Conduction and Ferromagnetic Properties in Titanium doped Fe_2VAl Thin Films. *Acta Mater.*, **2020**, *200*, 848-856.

(9) Chen, X.; Zhou, Z.; Lin, Y.; Nan, C. Thermoelectric Thin Films: Promising Strategies and Related Mechanism on Boosting Energy Conversion Performance. *J. Materiomics*, **2020**, *6*(3), 494-512.

(10) Shang, H.; Li, T.; Luo, D.; Yu, L.; Zou, Q.; Huang, D.; Xiao, L.; Gu, H.; Ren, Z.; Ding, F. High-Performance Ag-Modified $Bi_{0.5}Sb_{1.5}Te_3$ Films for the Flexible Thermoelectric Generator. *ACS Appl. Mater. Interfaces*, **2020**, *12*(6), 7358-7365.

(11) Ohkubo, I.; Hou, Z.; Aizawa, T.; Lippmaa, M.; Chikyow, T.; Tsuda, K.; Mori, T. Realization of Closed-loop

Optimization of Epitaxial Titanium Nitride Thin-Film Growth via Machine Learning. *Mater. Today Phys.*, **2021**, *16*, 100296.

(12) Xiao, N.; Zhu, L.; Wang, K.; Dai, Q.; Wang, Y.; Li, S.; Sui, Y.; Ma, Y.; Liu, J.; Liu, B.; Zou, G.; Zou, Bo. Synthesis and High-pressure Transformation of Metastable Wurtzite-structured $CuGaS_2$ Nanocrystals. *Nanoscale*, **2012**, *4*(23),7443-7447.

(13) Norako, M.E.; Brutchey, R.L. Synthesis of Metastable Wurtzite $CuInSe_2$ Nanocrystals. *Chem. Mater.*, **2010**, *22*(5), 1613-1615.

(14) Yin, D.; Dun, C.; Zhang, H.; Fu, Z.; Gao, X.; Wang, X.; Singh, D. J.; Carroll, D.L.; Liu, Y.; Swihart, M. T. Binary and Ternary Colloidal Cu-Sn-Te Nanocrystals for Thermoelectric Thin Films. *Small*, **2021**, *17*(11), 2006729.

(15) Tsujii, N.; Mori, T.. High Thermoelectric Power Factor in a Carrier-Doped Magnetic Semiconductor $CuFeS_2$. *Appl. Phys. Express*, **2013**, *6*(4), 043001.

(16) Tsujii, N.; Mori, T.; Isoda, Y. Phase Stability and Thermoelectric Propertiesof $CuFeS_2$-Based Magnetic Semiconductor. *J. Electron. Mater.*, **2014**, *43*, 2371-2375.

(17) Tsujii, N.; Meng, F.; Tsuchiya, K.; Maruyama, S.; Mori, T. Effect of Nanostructuring and High-Pressure Torsion Process on Thermal Conductivity of Carrier-Doped Chalcopyrite. *J. Electron. Mater.*, **2016**, *45*, 1642-1647.

(18) Takaki, H.; Kobayashi, K.; Shimono, M.; Kobayashi, N.; Hirose, K.; Tsujii, N.; Mori, T. Thermoelectric Properties of a Magnetic Semiconductor $CuFeS_2$. *Mater. Today Phys.*, **2017**, *3*, 85-92.

(19) Takaki, H.; Kobayashi, K.; Shimono, M.; Kobayashi, N.; Hirose, K.; Tsujii, N.; Mori, T. Seebeck Coefficients in $CuFeS_2$ Thin Films by First-principles Calculations. *Jpn. J. Appl. Phys.*, **2019**, *58*(SI), SIIB01.

(20) Sato, N.; Gan, P. S.; Tsujii, N.; Mori, T. Effect of Microstructure on Lattice Thermal Conductivity of Thermoelectric Chalcopyrite $CuFeS_2$: Experimental and Computational Studies. *Appl. Phys. Express*, **2021**, *14*(8), 087002.

(21) Xie, H.; Su, X.; Zheng, G.; Zhu, T.; Yin, K.; Yan, Y.; Uher, C.; Kanatzidis, M. G.; Tang, X. The Role of Zn in Chalcopyrite $CuFeS_2$: Enhanced Thermoelectric Properties of $Cu_{1-x}Zn_xFeS_2$ with In Situ Nanoprecipitates. *Adv. Energy Mater.*, **2017,** *7*(3), 1601299.

(22) Xie, H.; Su, X.; Hao, S.; Zhang, C.; Zhang, Z.; Liu, W.; Yan, Y.; Wolverton, C.; Tang, X.; Kanatzidis, M.G. Large Thermal Conductivity Drops in the Diamondoid Lattice of $CuFeS_2$ by Discordant Atom Doping. *J. Am. Chem. Soc.*, **2019**, *141*(47), 18900-18909.

(23) Xie, H.; Su, X.; Bailey, T.P.; Zhang, C.; Liu, W.; Uher, C.; Tang, X.; Kanatzidis, M. G. Anomalously Large Seebeck Coefficient of $CuFeS_2$ Derives from Large Asymmetry in the Energy Dependence of Carrier Relaxation Time. *Chem. Mater.*, **2020**, *32*(6), 2639-2646.

(24) Tomić, S.; Bernasconi, L.; Searle, B. G.; Harrison, N. M. Electronic and Optical Structure of Wurtzite $CuInS_2$. *J. Phys. Chem. C*, **2014**, *118*(26), 14478-14484.

(25) Xie, B.; Hu, B.; Jiang, L.; Li, G.; Du, Z. The Phase Transformation of $CuInS_2$ from Chalcopyrite to Wurtzite. *Nanoscale Res. Lett.*, **2015**, *10*, 1-7.

(26) Ghosh, S.; Avellini, T.; Petrelli, A.; Kriegel, I.; Gaspari, R.; Almeida, G.; Bertoni, G.; Cavalli, A.; Scotognella, F.; Pellegrino, T.; Manna, L. Colloidal $CuFeS_2$ Nanocrystals: Intermediate Fe d-Band Leads to High Photothermal Conversion Efficiency. *Chem. Mater.*, **2016**, *28*(13), 4848-4858.

(27) Poulose, A. C.; Zoppellaro, G.; Konidakis, I.; Serpetzoglou, E.; Stratakis, E.; Tomanec, O.; Beller, M.; Bakandritsos, A.; Zbořil, R. Fast and Selective Reduction of Nitroarenes under Visible Light with an Earth-Abundant Plasmonic Photocatalyst. *Nat. Nanotechnol.*, **2022**, *17*(5), 485-492.

(28) Ang, R.; Khan, A. U.; Tsujii, N.; Takai, K.; Nakamura, R.; Mori, T. Thermoelectricity Generation and Electron-Magnon Scattering in a Natural Chalcopyrite Mineral from a Deep-Sea Hydrothermal Vent. *Angew. Chem.*, **2015**, *127*(44), 13101-13105.

(29) Tsujii, N.; Nishide, A.; Hayakawa, J.; Mori, T. Observation of Enhanced Thermopower due to Spin Fluctuation in Weak Itinerant Ferromagnet. *Sci. Adv.*, **2019**, *5*(2), eaat5935.

(30) Ge, B.; Lee, H.; Zhou, C.; Lu, W.; Hu, J.; Yang, J.; Cho, S.; Qiao, G.; Shi, Z.; Chung, I. Exceptionally Low Thermal Conductivity Realized in the Chalcopyrite $CuFeS_2$ via Atomic-level Lattice Engineering. *Nano Energy*, **2022**, *94*, 106941.

(31) Xie, H.; Zhao, L. D.; Kanatzidis, M. G. Lattice Dynamics and Thermoelectric Properties of Diamondoid Materials. *Interdisciplinary Mater.*, **2024**, *3*(1), 5-28.

(32) Ji, M.; Liu, K.; Ji, N. Phases and Morphorlogy of $CuFeS_2$ Films Prepared by Electrodeposition. *J. Ceram. Process. Res.*, **2020**, *21*(4), 456-459.

(33) Malagutti, M. A.; Lohani, K.; D'Incau, M.; Nautiyal, H.; Ataollahi, N.; Scardi, P. Optimizing $CuFeS_2$ Chalcopyrite Thin Film Synthesis: A Comprehensive Three-Step Approach Using Ball-Milling, Thermal Evaporation, and Sulfurization Applied for Thermoelectric Generation. *Appl. Sci.*, **2023**, *13*(18), 10172.

(34) Chen, K.; Chiang, C.; Ray, D. Hydrothermal Synthesis of Chalcopyrite Using an Environmental Friendly Chelating Agent. *Mater. Lett.*, **2013**, *98*, 270-272.

(35) Barde, A.; Lewis, D. J. Fabrication of High Quality Bornite and Chalcopyrite Thin Films by Aerosol-Assisted Chemical Vapor Deposition. *J. Phys. Chem. C*, **2023**, *127*(28), 13969-13977.

(36) Barkat, L.; Hamdadou, N.; Morsli, M.; Khelil, A.; Bernede, J. C. Growth and Characterization of $CuFeS_2$ Thin Films. *J. Cryst. growth*, **2006**, *297*(2), 426-431.

(37) Jing, M.; Li, J.; Liu, K. Research Progress in Photolectric Materials of $CuFeS_2$. IOP Conference Series: Earth and Environmental Science, **2018**, *128*(1), 012087.

(38) Hinterleitner, B.; Knapp, I.; Poneder, M.; Shi, Y.; Müller, H.; Eguchi, G.; Eisenmenger-Sittner, C.; Stöger-Pollach, M.; Kakefuda, Y.; Kawamoto, N.; Guo, Q.; Baba, T.; Mori, T.; Ullah, S.; Chen, X.; Bauer, E. Thermoelectric

Performance of a Metastable Thin-film Heusler Alloy. *Nature*, **2019**, *576*(7785), 85-90.

(39) Pang, H.; Bourgès, C.; Jha, R.; Baba, T.; Sato, N.; Kawamoto, N.; Baba, T.; Tsujii, N.; Mori, T. Revealing an Elusive Metastable Wurtzite $CuFeS_2$ and the Phase Switching between Wurtzite and Chalcopyrite for Thermoelectric Thin Films. *Acta Mater.*, **2022**, *235*, 118090.

(40) Izumi, F.; Momma, K. Three-Dimensional Visualization in Powder Diffraction. *Solid State Phenomena*, **2007**, *130*,15-20.

(41) Sahin, G.; Goktas, A.; Aslan, E. A New Way to Tune Photocatalytic Activity, Surface Morphology, and Structural/Optical Parameters of ZrO_2 Thin Films Using Different Zr Sources along with Annealing Temperature and Film Thickness, *J. Sol-Gel Sci. Technol.* **2024**, 1-19.

(42) Goktas, A.; Modanlı, S.; Tumbul, A.; Kilic, A. Facile Synthesis and Characterization of ZnO, ZnO: Co, and ZnO/ZnO: Co Nano Rod-like Homojunction Thin Films: Role of Crystallite/Grain Size and Microstrain in Photocatalytic Performance. *J. Alloys Compd.*, **2022**, *893*, 162334.

(43) Goktas, A. Sol–gel Derived $Zn_{1-x}Fe_xS$ Diluted Magnetic Semiconductor Thin Films: Compositional Dependent Room or Above Room Temperature Ferromagnetism. *Appl. Surf. Sci.*, **2015**, *340*, 151-159.

(44) Sahin, G.; Goktaş, S. Calculations of Structural Parameters and Optical Constants of Size Dependent ZrO_2. Gazi J. Eng. Sci., **2024**, *10* (1), 114-124.

(45) Aba, Z.; Goktas, A.; Kilic. Characterization of $Zn_{1-x}La_xS$ Thin Films; Compositional, Surface, Optical, and Photoluminescence Properties for Possible Optoelectronic and Photocatalytic Applications. *J. Sol-Gel Sci. Technol.*, **2024**, *109* (1), 260-271.

(46) Knight, K. S.; Marshall, W. G.; Zochowski, S. W. The Low-Temperature and High-Pressure Thermoelastic and Structural Properties of Chalcopyrite, $CuFeS_2$. *Canad. Mineral.*, **2011**, *49*(4), 1015-1034.

(47) Exner, G.; Schunemann, P. G.; Ivanova, E.; Grigorov, A.; Petrov, V. Nanohardness and Young's Modulus of II-IV-V_2 Chalcopyrite Nonlinear Optical Crystals: A Comparative Study. *Opt. Mater. Express*, **2024**, *14* (4), 1039-1047.

(48) Weiss, V.; Bohne, W.; Röhrich, J.; Strub, E.; Bloeck, U.; Sieber, I.; Ellmer, K.; Mientus, R.; Porsch, F. Reactive Magnetron Sputtering of Molybdenum Sulfide Thin Films: In situ Synchrotron X-ray Diffraction and Transmission Electron Microscopy Study. *J. Appl. Phys.*, **2004**, *95*(12), 7665-7673.

(49) Wang, C.; Xue, S.; Hu, J.; Tang, K. Raman, Far Infrared, and Mössbauer Spectroscopy of $CuFeS_2$ Nanocrystallites. *Jpn. J. Appl. Phys.*, **2009**, *48*(2R), 023003.

(50) Y. C. Cheng, C. Q. Jin, F. Gao, X. L. Wu, W. Zhong, S. H. Li, Paul K. Chu. Raman scattering study of zinc blende and wurtzite ZnS. *J. Appl. Phys*, **2009**, *106*(12), 123505.

(51) Tonpe, D.; Gattu, K.; More, G.; Upadhye, D.; Mahajan, S.; Sharma, R. Synthesis of $CuFeS_2$ Thin Films from Acidic Chemical Baths. *AIP Conference Proceedings*. **2016**, *1728*(1), 020676.

(52) Guo, S.; Du, Z.; Dai, S. Analysis of Raman Modes in Mn-doped ZnO Nanocrystals. *Phys. Status Solidi (b)*, **2009**, *246*(10), 2329-2332.

(53) Dean, J. A. Lange's handbook of chemistry. (1999).

(54) Steimle, B. C.; Lord, R. W.; Schaak, R. E.. Phosphine-Induced Phase Transition in Copper Sulfide Nanoparticles Prior to Initiation of a Cation Exchange Reaction. *J. Am. Chem. Soc.*, **2020**, **142**(31), 13345-13349.

(55) Wang, Y.; Pang, H.; Guo, Q.; Tsujii, N.; Baba, T.; Baba, T.; Mori, T. Flexible n-Type Abundant Chalcopyrite/PEDOT:PSS/Graphene Hybrid Film for Thermoelectric Device Utilizing Low-Grade Heat. *ACS Appl.Mater. Interfaces*, **2021**, *13*(43), 51245-51254.

(56) Jones, W.; March, N.H. Theoretical solid state physics. (Vol. 35) Courier Corporation, 1985.

TOC Graphic

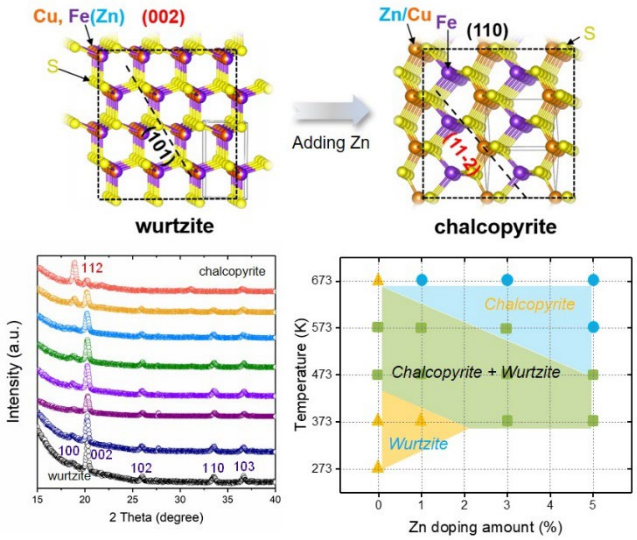
Cu, Fe(Zn) (002)
S
(101)
wurtzite
Adding Zn
Zn/Cu
Fe
(110)
S
(11-2)
chalcopyrite
Intensity (a.u.)
112
chalcopyrite
100
002
102
110
103
wurtzite
15
20
25
30
35
40
2 Theta (degree)
Temperature (K)
673
573
473
373
273
Chalcopyrite
Chalcopyrite + Wurtzite
Wurtzite
0
1
2
3
4
5
Zn doping amount (%)